

基于 SPR 和干涉模式复合增强窄带钙钛矿光电探测器

何剑涛^{1,2}, 吕且妮^{1,2*}, 张明娣^{1,2}, 戴海涛^{3,4}, 付宜凯^{3,4}, 陈小鹏^{1,2}¹天津大学精密仪器与光电子工程学院, 天津 300072;²天津大学光电信息技术教育部重点实验室, 天津 300072;³天津大学理学院, 天津 300072;⁴天津大学天津市低维功能材料物理与制备技术重点实验室, 天津 300072

摘要 制备了一种基于银岛膜表面等离子共振的窄带钙钛矿光电探测器,通过钙钛矿与银岛膜之间的薄膜干涉实现了窄带增强。利用前驱液温度调控晶粒尺寸,通过钙钛矿厚度调控光传播路径,增强了窄带响应,实现了中心波长为 490 nm、峰值半峰全宽为 110 nm 的窄带光探测,其上升和下降时间分别为 247 ms 和 266 ms,响应光电流为 0.151 μA ,外量子效率为 159%,响应度为 0.6 $\text{A} \cdot \text{W}^{-1}$,归一化探测率为 $2.73 \times 10^{13} \text{ cm} \cdot \text{Hz}^{1/2} \cdot \text{W}^{-1}$ 。

关键词 测量;窄带光电探测器;前驱液温度优化;表面等离子共振;薄膜干涉

中图分类号 TN303

文献标志码 A

DOI: 10.3788/CJL202249.2304004

1 引言

窄带光电探测器在彩色图像识别、机器视觉、生物传感和图像处理等领域中有着广阔的应用前景。传统窄带光电探测器通常是利用光学滤波器从宽带光电探测器中获得某一波长,该方法的结构复杂,成本高,且降低了探测器的灵敏度^[1]。随后基于不同原理的无滤光片的窄带光电探测器制备方法被提出,这些原理包括基于窄带吸收材料^[2]、电荷收集窄带 (CCN) 概念^[3]、等离子体效应^[4]、钙钛矿与聚合物协同效应^[5-6]等。如 Gao 等^[2]基于有机染料 [氟硼二吡咯 (BODIPY)染料]窄带吸收特性,制备了一种基于有机染料/ $\text{Zn}_{0.9}\text{Mg}_{0.1}\text{O}$ 纳米粒子/石墨烯结构的中心波长为 530 nm 的高响应度的窄带光电探测器。文献^[3]基于 CCN 概念,在钙钛矿上制备了一种峰值半峰全宽小于 100 nm 的可调谐的红、绿、蓝三个波段的窄带光电探测器。基于金属纳米颗粒 (MNP) 增强的钙钛矿 (PVSK) 窄带光电器件,结合了 MNP 的光场增强和 PVSK 优秀的光电性能 (吸收系数高、载流子分离距离长、迁移率高、光学带隙可调等)^[7-13],是目前太阳能电池^[14-16]、光电探测器^[17-18]等领域的研究热点。其中,将 MNP 制备于衬底表面^[19,20]的钙钛矿器件,制备方式简单,但 PVSK 和 MNP 直接接触导致钙钛矿成膜质量下降^[21],解决这一问题的方法之一是在 PVSK 和 MNP 之间引入中间层,以改善成膜质量。如 Liu

等^[21]通过低温喷雾化学气相沉积法,将银纳米颗粒沉积在 FTO 玻璃 (掺杂氟的 SnO_2 导电玻璃) 表面,并将 TiO_2 作为中间层制备了超薄的钙钛矿太阳能电池。Sun 等^[19]通过单层的自组装 3-氨基丙基三甲氧基硅烷,将金纳米颗粒固定在 Si/SiO_2 基底上,隔开了金纳米颗粒与钙钛矿。文献^[22]将银纳米颗粒嵌入 10 nm 厚的 SiO_2 薄层中,银纳米颗粒- SiO_2 薄层与钙钛矿间用石墨烯隔开,制备得到的器件具有高的光响应增强因子。这些中间层的制备相对困难,且成本高。聚甲基丙烯酸甲酯 (PMMA) 具有制备简单、成本低、可见光范围内光透过率高等特点^[23],是钙钛矿器件中常用的光学塑料薄膜,在器件封装^[24]、稳定性提高^[25]等方面有重要应用。

本文基于气相沉积和退火工艺,在玻璃衬底表面上制备了银纳米岛膜,利用银纳米粒子表面等离子共振 (SPR) 效应实现窄带探测,引入 PMMA 薄膜作为钙钛矿和银岛膜之间的中间层,利用光经过 PMMA 薄膜的干涉效应增强窄带,通过前驱液温度和钙钛矿厚度调控窄带响应,制备了高性能的银纳米岛膜基的窄带光电探测器。

2 钙钛矿窄带光电探测器的制备及机理

2.1 银岛膜的制备及窄带光电探测

先对玻璃衬底进行预处理。利用洗洁精清洗玻璃

收稿日期: 2021-12-10; 修回日期: 2022-02-26; 录用日期: 2022-04-08

基金项目: 基础加强项目 (2019-JCJQ-ZD-282-00)

通信作者: *qienil@tju.edu.cn

基板表面,去离子水超声清洗两次,每次 15 min,乙醇超声清洗 20 min,完成清洗过程。再用臭氧对清洗的玻璃基板处理 30 min,使其钝化,采用物理气相沉积(PVD)方法在该基底上蒸镀 8 nm 厚度的银薄膜。将所制备的银薄膜在氮气环境中 300 °C 下退火 30 min,得到银岛膜,如图 1 所示。图 2(a)、(b)为银岛膜的扫

描电镜(SEM)图,退火后的银纳米粒子呈球形和半球形,均匀分布,直径约为 80 nm。图 2(c)~(e)中实线为银岛膜的透射谱、反射谱和吸收谱,在 427 nm 处,吸收谱和反射谱均达到最大值,透射谱为最小值,且带宽很小,银岛膜在 427 nm 附近有很好的窄带滤波作用。

基于银岛膜的窄带滤波是基于银纳米粒子的表面等离子激元效应。光入射到银岛膜上,银表面的自由电子与入射光子相互作用,使表面自由电子被激发,诱导产生 SPR,SPR 产生强烈的光吸收,极大地增强了银纳米颗粒的表面局域电场。我们已经利用基于银纳米颗粒的 SPR 实现了钙钛矿光电探测器光电流的增强^[26]。图 2(c)~(e)中虚线为基于 COMSOL 软件计算得到的颗粒半径为 40 nm、颗粒间距为 2 nm 的球形银岛膜的透射谱、反射谱和吸收谱。图 2(f)为 420 nm 波长处的电场分布,银颗粒上的正负电荷形成振荡偶

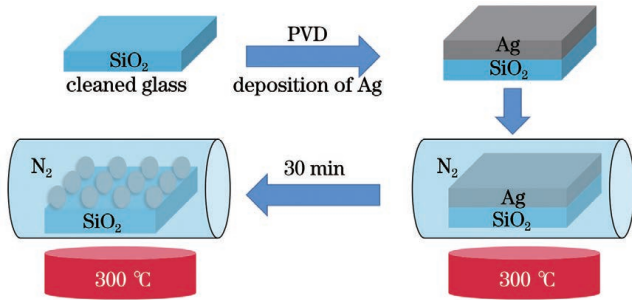


图 1 银岛膜制备示意图

Fig. 1 Schematic of silver island film preparation

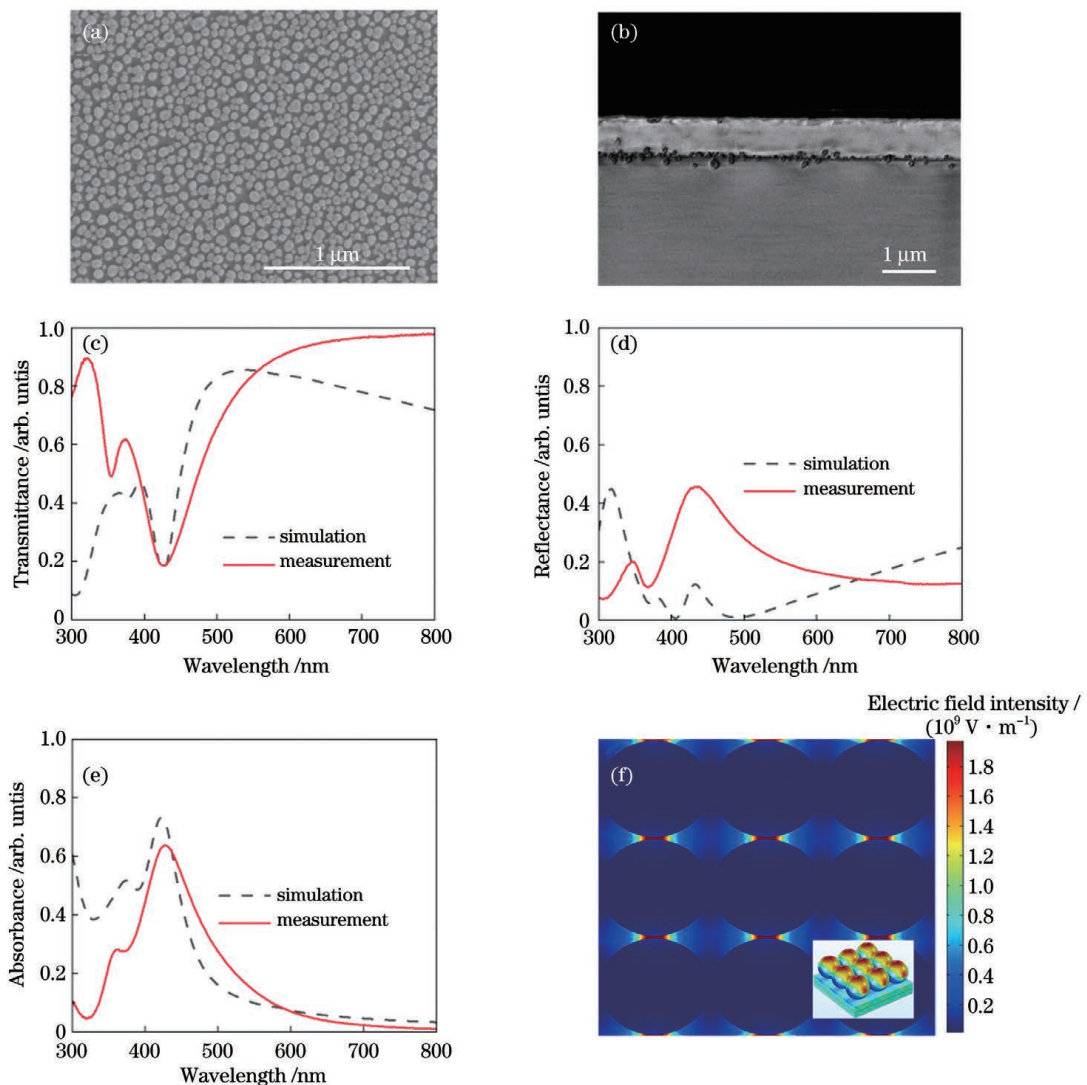


图 2 银岛膜表征和仿真。(a)银岛膜的 SEM 图;(b)银岛膜/钙钛矿界面处的截面 SEM 图;银岛膜的(c)透射谱、(d)反射谱和(e)吸收谱;(f)共振处的电场(俯视图)和计算模型(插图)

Fig. 2 Characterization and simulation of silver island film. (a) SEM image of silver island film; (b) SEM of section at silver island film/perovskite interface; (c) transmission spectra, (d) reflectance spectra, and (e) absorption spectra of silver island film; (f) electric field at resonance (top view) and calculation model (insert)

极子,在颗粒间隙处形成了增强的 SPR,对 420 nm 波长光有很强的吸收,透射率很低,实现了光谱滤波。忽略模型和测量误差,模拟结果与实验结果吻合。银岛膜产生了 SPR,具有很好的窄带滤波效果。

2.2 PMMA 薄膜制备及窄带增强

图 3(a)为基于银岛膜的钙钛矿窄带探测器制备

示意图,其结构包括银岛膜、PMMA 薄膜和钙钛矿。采用一步旋涂方法在所制备的银岛膜上旋涂 PMMA 薄膜,改善银岛膜与钙钛矿的接触界面。再在 PMMA 上旋涂钙钛矿前驱液,利用气相沉积法,在钙钛矿上蒸镀 100 nm 厚的银电极。

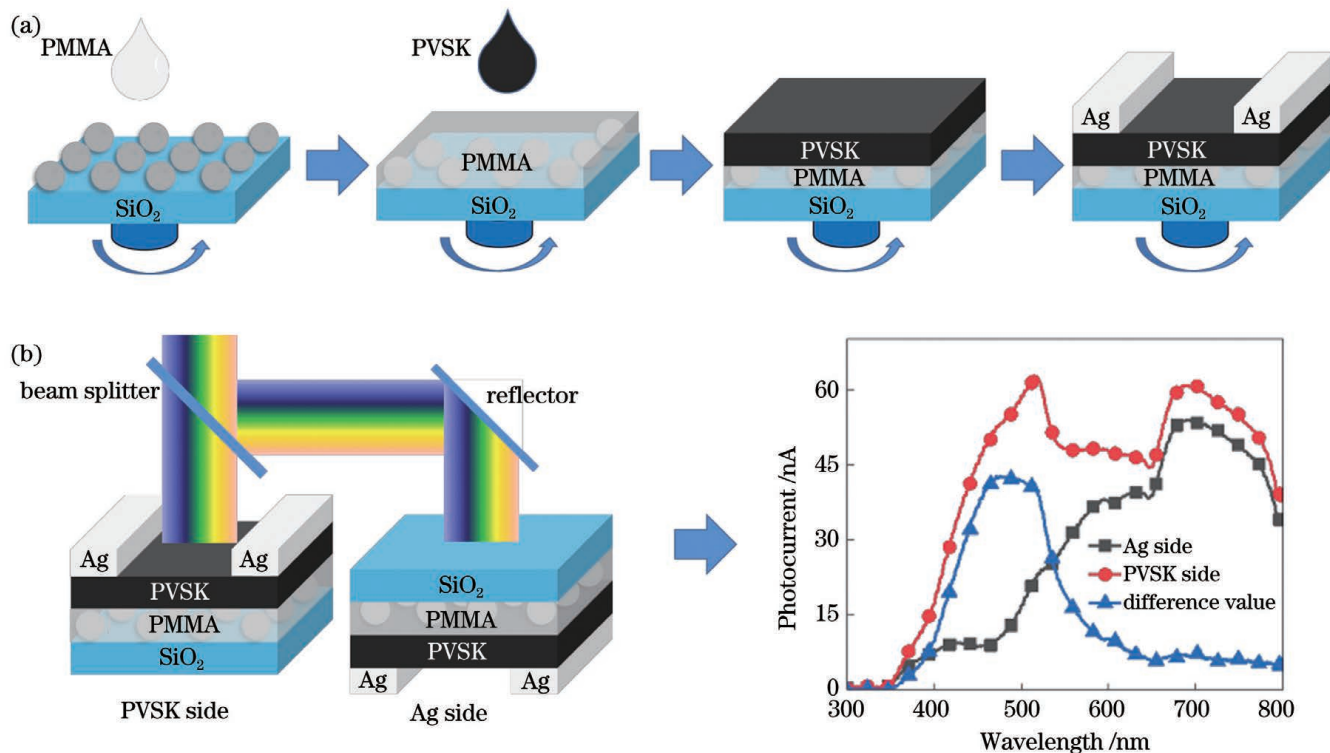


图 3 器件制备及工作原理。(a)钙钛矿光电探测器的制备示意图;(b)窄带光电探测器的工作原理

Fig. 3 Fabrication and operating principle of device. (a) Schematic of fabrication of perovskite photodetector; (b) operation principle of narrowband photodetector

图 3(b)为窄带光电探测器的工作原理。入射光经过分光器后被分为两束光,分别从探测器顶部和底部入射。光沿 PVSK→PMMA→银岛膜入射,称为钙钛矿侧入射;光沿银岛膜→PMMA→PVSK 入射,称为银岛膜侧入射。对于钙钛矿侧入射,由于钙钛矿具有非常强的吸收,到达银岛膜层的光相对很弱,忽略银岛膜的反射作用,这时探测的谱线为钙钛矿本征波长响应谱。对于银岛膜侧入射,由于银岛膜对特定波长光的局域增强^[27],到达钙钛矿吸收层的特定波长光减少,银岛膜对应特征波长处的响应减弱,这时探测的谱线为经过消光后的特征谱线。将这两个波长处的电流谱的差作为窄带响应谱。经过 PMMA 薄膜上下表面的反射光/透射光发生干涉,影响入射光的透过率,其中心波长与薄膜厚度相关。

2.3 PMMA 膜厚对窄带探测的影响

在图 3(a)中,当旋涂速度和 PMMA 溶液浓度不同时,银岛膜表面旋涂的 PMMA 薄膜厚度不同。图 4(a)给出了不同 PMMA 厚度下的窄带响应谱,图 4(b)为不同 PMMA 厚度下窄带响应谱的峰值半峰

全宽(FWHM)和光电流。从图 4(a)、(b)可以看出,窄带响应谱的中心波长在 490 nm 附近,随着 PMMA 厚度的增加,FWHM 和光电流先增大后减小,在 71~278 nm 区间,FWHM 变化较小,在 278 nm 处 FWHM 较窄,宽度为 128 nm,光电流有最大值,为 45 nA。图 4(c)为不同厚度 PMMA 的银岛膜透射谱。由于 PMMA 的引入,银岛膜最低透过率波长发生红移,由 427 nm(无 PMMA)移动到了 470 nm 左右,最低透过率由 18%减小到 9%左右,随着 PMMA 厚度的增加,最低透率先减小后增大,在 278 nm 厚度处达到最小值(9%),对应于图 4(a)。这是因为厚度为 278 nm 时,入射光在 PMMA 薄膜上发生干涉相消,透过率最低。图 4(d)为银岛膜和旋涂了不同厚度 PMMA 的钙钛矿的 X 射线衍射(XRD)谱,图 4(e)为(110)衍射峰的放大图。引入了银岛膜和 PMMA 的钙钛矿薄膜仍具有钙钛矿的特征峰。PMMA 的引入提高了(110)衍射峰的强度,钙钛矿的结晶性增强,824 nm 厚度下钙钛矿具有最优的结晶度,但 278 nm 厚度下钙钛矿有更好的窄带响应。因此,选 278 nm 为 PMMA 最优厚度。

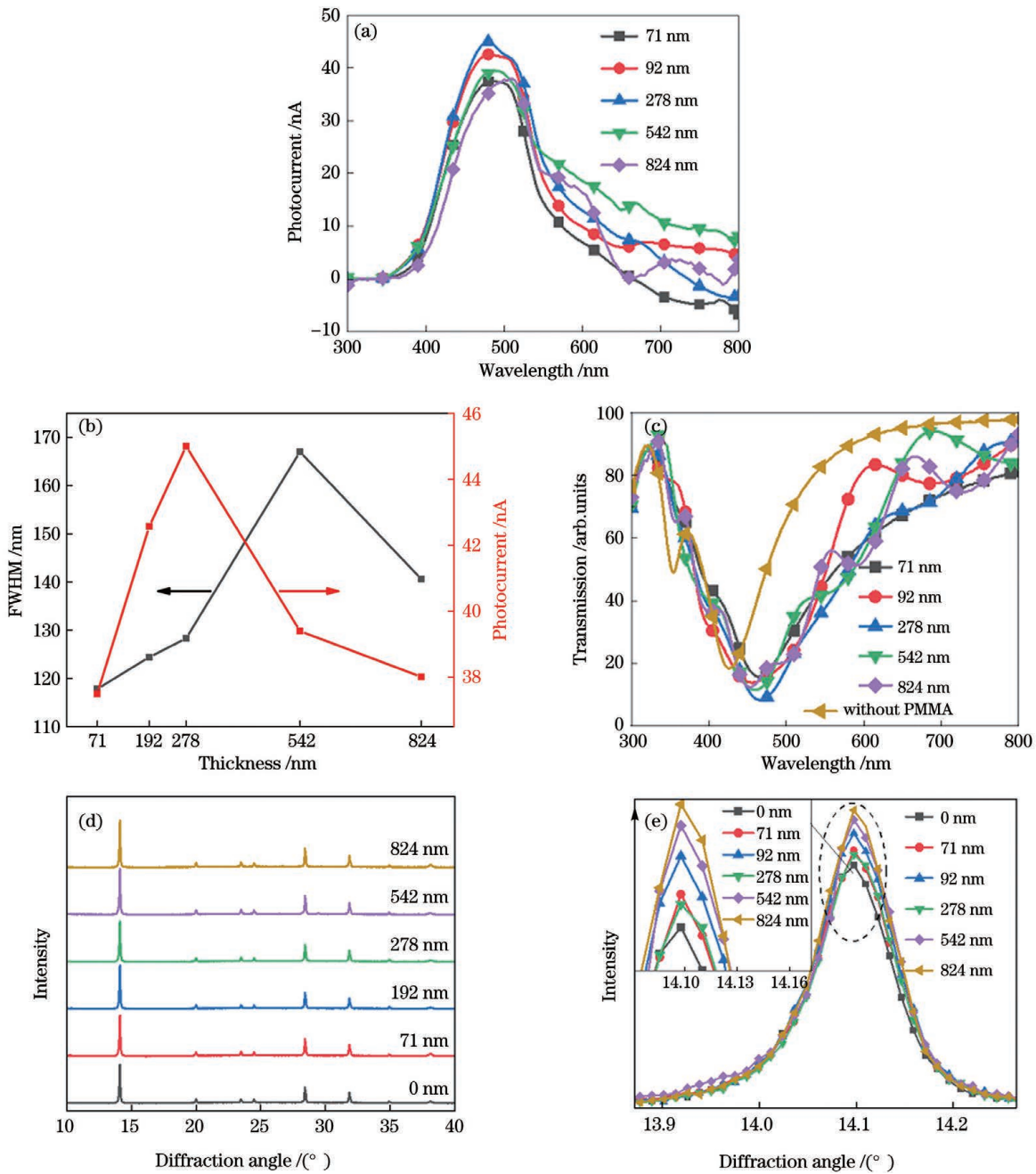


图 4 不同 PMMA 厚度下器件的表征。(a)窄带响应随波长的变化;(b)钙钛矿器件的 FWHM 和光电流;(c)银岛膜的透射谱;(d)钙钛矿薄膜的 XRD 谱;(e) (110) 衍射峰的放大图

Fig. 4 Characterization of devices under different PMMA thicknesses. (a) Narrowband response versus wavelength; (b) FWHM and photocurrent of perovskite device; (c) transmission spectra of silver island films; (d) XRD spectra of perovskite films; (e) magnified view of (110) diffraction peak

3 器件性能优化

PMMA 薄膜改善了 PVSK-MNP 的接触界面,且通过 PMMA 薄膜的干涉实现了窄带效应增强,但相比于玻璃基底的 PVSK,PMMA 影响了钙钛矿的成膜质量,光电流降低。这里分析前驱液温度和钙钛矿厚度对探测器性能的影响。

3.1 前驱液温度

对于给定的晶体,结晶成核过程中的临界半径 r_c 是 ΔT 的函数^[28]:

$$r_c \propto (\Delta T)^{-1}, \quad (1)$$

式中: $\Delta T = T - T^*$,其中 T 为实际温度, T^* 为晶体的固液平衡温度。由式(1)可知,利用温度可对钙钛矿的晶粒尺寸进行优化。

将钙钛矿前驱液置于加热台上加热,利用温度枪测量前驱液的温度。用移液枪取 100 μL 钙钛矿前驱液置于旋涂仪上,设定 3 s 内的转速为 500 r/min,60 s 内的转速为 3000 r/min。图 5(a)~(f) 分别给出了不同前驱液温度下钙钛矿的 SEM 形貌图。可以看出:随温度的升高,钙钛矿晶粒尺寸 r_c 增大;60 $^\circ\text{C}$ 时粒径

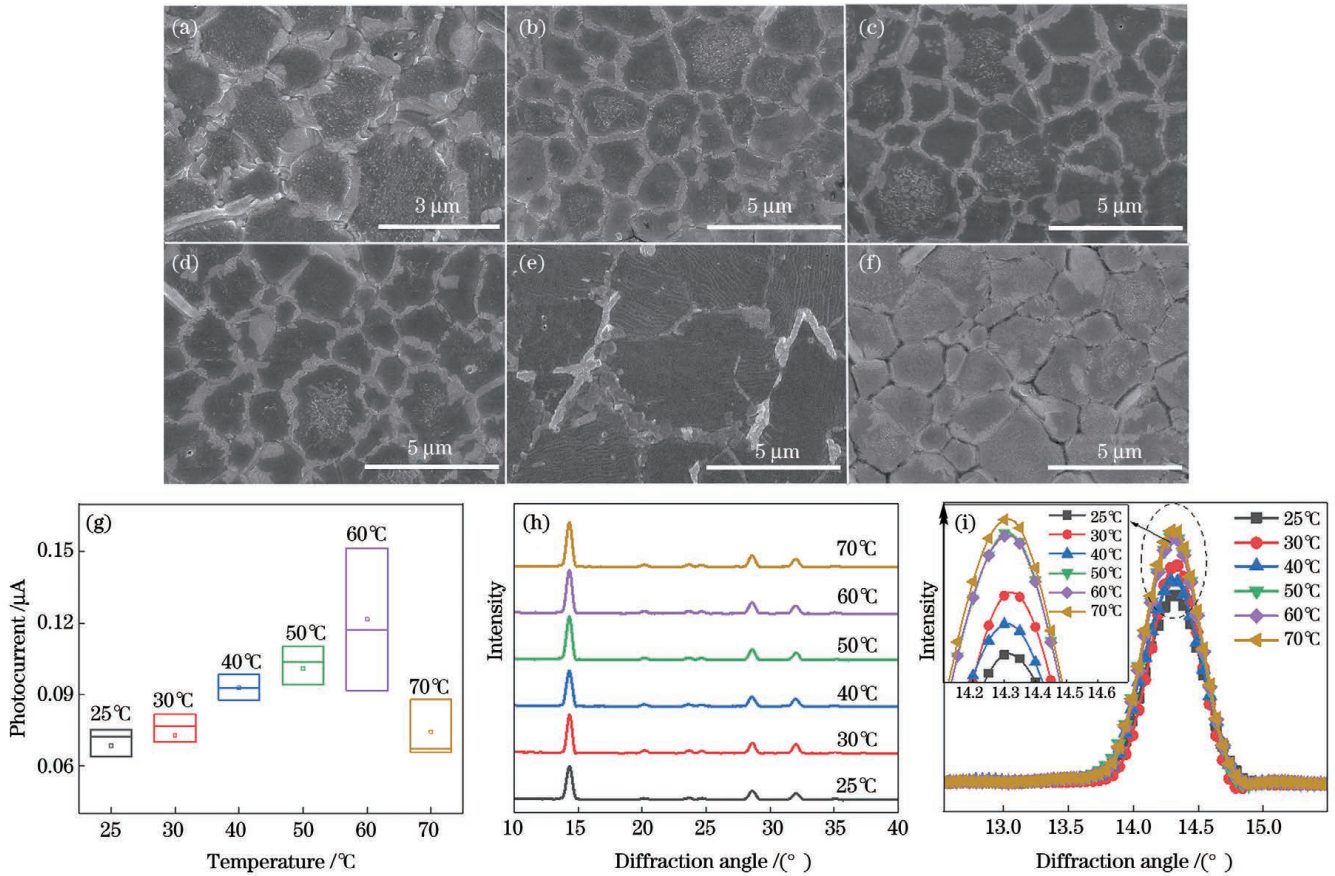


图 5 不同前驱液温度下器件的表征。前驱液温度分别为(a)室温(~25 °C)、(b)30 °C、(c)40 °C、(d)50 °C、(e)60 °C和(f)70 °C时钙钛矿的 SEM 图;(g)入射光波长为 550 nm 时光电流随前驱液温度的变化;(h)不同前驱液温度下钙钛矿薄膜的 XRD 谱;(i) (110)衍射峰的放大图

Fig. 5 Characterizations of device under different precursor solution temperatures. SEM images of perovskite when temperature of precursor solution is (a) room temperature (~25 °C), (b) 30 °C, (c) 40 °C, (d) 50 °C, (e) 60 °C, and (f) 70 °C, respectively; (g) photocurrent versus temperature of precursor solution when wavelength of incident light is 550 nm; (h) XRD spectra of perovskite films under different precursor solution temperatures; (i) magnified view of (110) diffraction peak

达到最大,约为 5 μm,且晶界较少[图 5(e)], ΔT 达到最小; $T=70$ °C时,粒径减小,晶界处出现较大的空隙[图 5(f)]。图 5(g)给出了不同前驱液温度下的探测器光电流。随着前驱液温度的升高,光电流先增大再减小。这是因为随着温度的升高,晶粒尺寸 r_c 增大,晶界减少,载流子的传输能力增强,60 °C时 r_c 最大,随后晶粒尺寸 r_c 减小,晶界处出现空隙,阻碍了钙钛矿内载流子的传输,光电流减小。

图 5(h)为不同前驱液温度下钙钛矿薄膜的 XRD 谱,其在 14°和 28°衍射角处均有较强的衍射峰,这表明所制备的薄膜具有良好的结晶度。图 5(i)给出了 14°衍射角处(110)的衍射峰。可以看出,加热前驱液有助于制备更高结晶质量的钙钛矿薄膜,温度越高,结晶度越高。结合载流子传输的能力,本实验中最优的前驱液处理温度选为 60 °C。

3.2 钙钛矿薄膜厚度的优化

图 6(a)为不同钙钛矿薄膜厚度下器件内入射光的传播路径示意图,其中 PMMA 薄膜厚度为 278 nm。对于钙钛矿侧入射,当吸光层(PMMA 和钙钛矿薄膜)

较厚时,光很难穿过吸光层到达底部的银岛膜层,此时吸光层对入射光只产生一次吸收。当吸光层较薄时,光穿过吸光层到达底部的银岛膜层,经银岛膜反射,反射光进入吸光层,加强了特征波长的光吸收。对于银岛膜侧入射,当吸光层较厚时,光只进入到吸光层的浅表面,产生的光生载流子距离银电极较远,很难被探测。当吸光层较薄时,光在更靠近银电极的位置处产生光生载流子,从而提高了器件响应。在实验中,通过控制旋涂速度,控制钙钛矿薄膜层的厚度,转速越大,薄膜越薄。

图 6(b)给出了不同旋涂速度下钙钛矿侧入射时器件的光电流随波长的变化曲线,其中前驱液温度为 60 °C,PMMA 厚度为 278 nm。随着旋涂速度的增大,光电流先增加再减小,在旋涂速度为 4000 r/min 时得到最大值。同时,随着转速的增加,在 520 nm 波长附近(虚线区域),较高旋涂速度下器件出现了光电流增强的现象。为了更好说明这一现象,引入了标准的硅探测器的归一化光电流谱,如图 6(c)所示。当旋涂转速大于 4000 r/min 时,吸光层较薄,在 520 nm

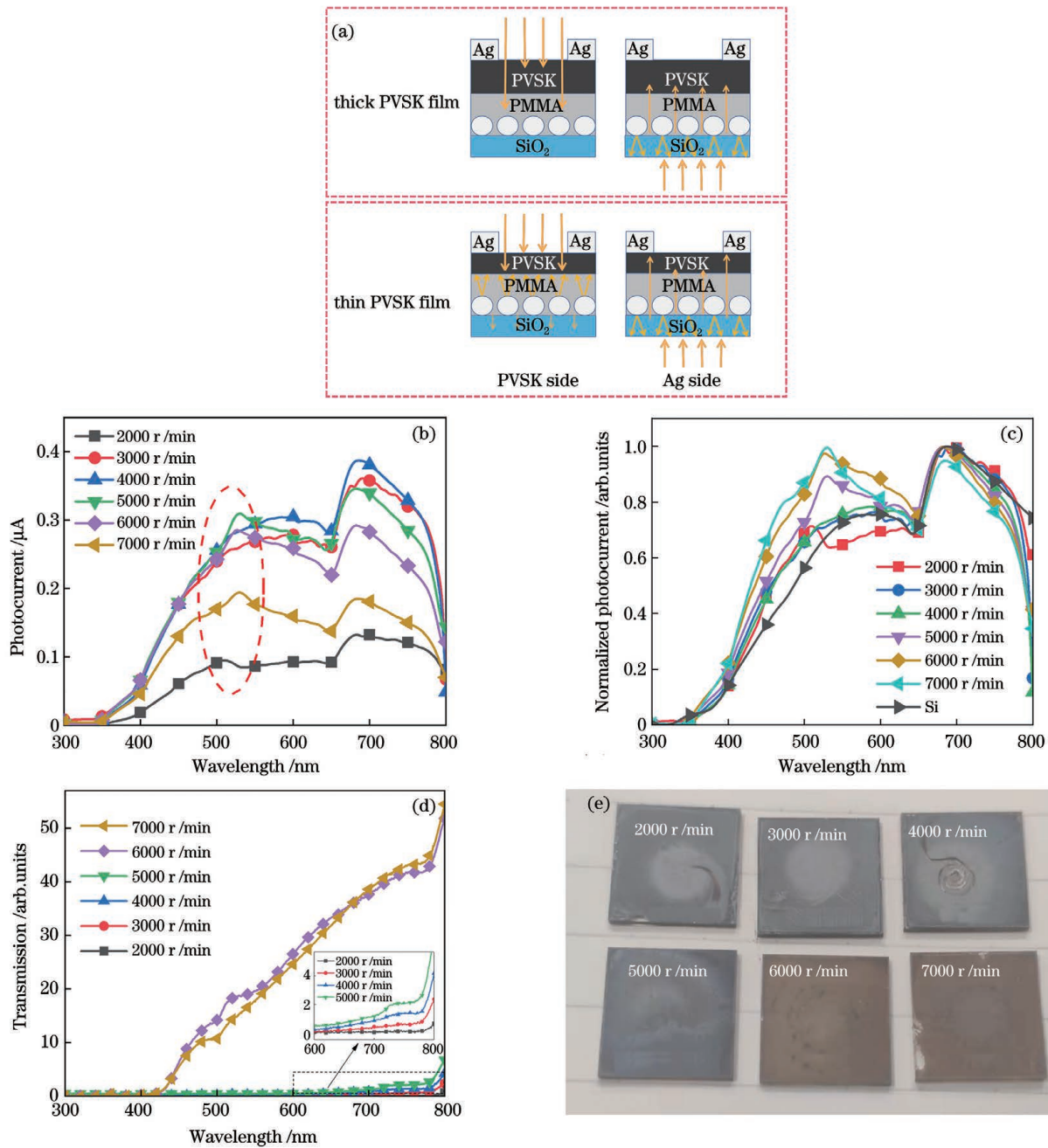


图 6 旋涂速度对光传播路径和光电流的影响。(a)钙钛矿薄膜内光传播的路径示意图;(b)不同旋涂速度下光电流随波长的变化;(c)归一化光电流曲线和 Si 探测器的光电流曲线;(d)不同旋涂速度下的透射谱;(e)不同旋涂速度下样品的光学图像
 Fig. 6 Effects of spin-coating speed on light propagation path and photocurrent. (a) Schematic of light propagation path in perovskite film; (b) photocurrent versus wavelength under different spin-coating speeds; (c) normalized photocurrent curves and photocurrent curve of Si detector; (d) transmission spectra under different spin-coating speeds; (e) optical images of samples under different spin-coating speeds

波长附近有明显的光电流增强。这是入射光在银岛膜处的反射引起的,反射光进入吸光层使该波长处的光电流增强。当旋涂转速小于 4000 r/min 时,吸光层较厚(约为 1.24 μm),在靠近 PMMA 侧反射光几乎被完全吸收,此时产生的载流子无法到达银电极处,不能被检测到,故光电流不高。考虑到窄带响应中心波长在 490 nm 附近,将 5000 r/min 选为最优的钙钛矿旋涂速度。图 6(d)为不同旋涂速度下的样品透射谱。随着旋涂速度的增加,透过率增大,在旋

涂速度大于 5000 r/min(约 843 nm 波长)后,透过率急剧增大。如在中心波长 680 nm 处,旋涂速度为 5000 r/min 时的透过率为 1%,旋涂速度为 6000 r/min 时的透过率为 36%。图 6(e)为不同旋涂速度下的样品光学图像。可以看出,旋涂速度为 6000 r/min 和 7000 r/min 时透明度明显较高,能看到背景中的直线。

3.3 器件性能测试

为了进一步探究此窄带光电探测器的工作性能,

对其进行了性能评估测试。当入射光波长为 550 nm、偏压为 2 V 时,最优参数的探测器开关特性(记为样品 2)如图 7(a)所示,其中 PMMA 厚度为 278 nm,前驱液温度为 60 °C,钙钛矿旋涂速度为 5000 r/min。为了便于比较,给出了未优化的样品开关特性(记为样品 1),其中 PMMA 厚度为 278 nm,前驱液温度为 25 °C(室温),钙钛矿旋涂速度为 3000 r/min。在较长的时间周期中,光电流稳定,开关比分别为 156 和 59。图 7(b)为一个开关周期内的探测器开关特性,未优化样品 1 的上升时间为 352 ms,下降时间为 389 ms,优化后样品 2 的上升时间约为 247 ms,下降时间约为 266 ms,具有快速的响应速度。图 7(c)、(d)为 2 V 偏

压下的器件窄带响应谱和外量子效率(EQE)与波长的关系曲线。对于最优样品 2,在波长 470 nm 附近有 159% 的高外量子效率,在 490 nm 附近有最大光电流,为 0.151 μA ,FWHM 为 110 nm。对于未优化样品 1,其外量子效率约为 48%,最大光电流为 0.04 μA ,FWHM 为 127 nm。图 7(e)、(f)为不同波长下的响应度(R)和归一化探测率(D^*),在 470 nm 波长附近,样品 2 的响应度为 0.6 $\text{A} \cdot \text{W}^{-1}$,归一化探测率为 $2.73 \times 10^{13} \text{ cm} \cdot \text{Hz}^{1/2} \cdot \text{W}^{-1}$,分别优于样品 1 的 0.188 $\text{A} \cdot \text{W}^{-1}$ 和 $8.53 \times 10^{12} \text{ cm} \cdot \text{Hz}^{1/2} \cdot \text{W}^{-1}$ 。说明温度优化和吸光层厚度的优化提高了样品的光电性能和窄带响应。

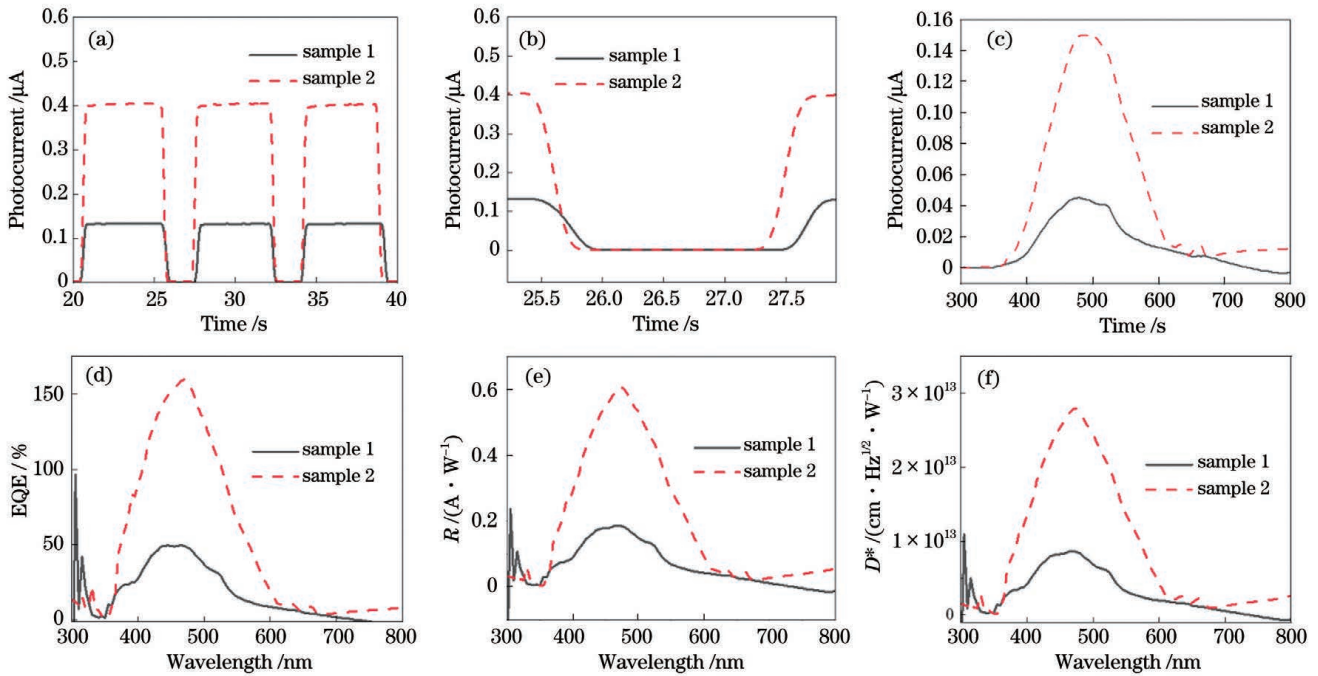


图 7 器件的表征。(a)完整和(b)单个开关周期下的光电流;(c)光电流;(d)外量子效率;(e)响应度;(f) 归一化探测率
Fig. 7 Device characterizations. Photocurrent under (a) complete or (b) single switching period; (c) photocurrent; (d) external quantum efficiency; (e) responsivity; (f) normalized detectivity

表 1 对比了所制备的窄带光电探测器与目前已报道的窄带光电探测器的性能参数,其中 t_{on} 为上升时间, t_{off} 为下降时间。可以看到,与其他器件相比,本文所制备的窄带光电探测器的归一化探测率最高达

$2.73 \times 10^{13} \text{ cm} \cdot \text{Hz}^{1/2} \cdot \text{W}^{-1}$,外量子效率也较高,但响应速度和 FWHM 较差。相比于 CsPbBr_3 ^[7] 等单晶器件复杂的制备工艺和高昂的制造成本,本文所提的旋涂法制备工艺具有一定优势。

表 1 窄带光电探测器的性能对比

Table 1 Performance comparison of narrowband photodetectors

Photodetector	Wavelength /nm	EQE /%	$R / (\text{A} \cdot \text{W}^{-1})$	$D^* / (\text{cm} \cdot \text{Hz}^{1/2} \cdot \text{W}^{-1})$	FWHM /nm	$t_{\text{on}}/t_{\text{off}}$	Ref.
UPSQ	500	16	—	—	90	—	[29]
Organic dye/Zn _{0.9} Mg _{0.1} O/nanoparticle/graphene	530	1.87×10^4	8×10^3	1.7×10^{12}	60	—	[2]
CsPbBr ₃	545	11	0.05	4×10^{11}	12	0.4 ms/2.3 ms	[7]
Au/CsPbBr ₃ /C ₆₀ /BCP/Ag	550	50	—	6.5×10^{10}	16	—	[30]
Cs ₃ Sb ₂ Br ₉	480	1.8×10^3	2.29	3.77×10^{12}	15	<0.2 ms	[31]
This work	490	160	0.6	2.73×10^{13}	110	247 ms/266 ms	

4 结 论

基于银岛膜产生的电场局域增强效应实现了窄带滤波,利用光经过 PMMA 薄膜后的干涉效应增强了窄带效应,通过前驱液温度和钙钛矿厚度调控了窄带响应,并制备了高性能的银纳米岛膜基窄带光电探测器。分析了 PMMA 薄膜厚度、前驱液温度和钙钛矿厚度对探测器性能的影响,优化了器件参数,实现了中心波长为 490 nm、FWHM 为 110 nm 的窄带探测。在 2 V 的外加偏压下,所制备的窄带光电探测器在响应峰处具有高达 $0.6 \text{ A} \cdot \text{W}^{-1}$ 的响应度、159% 的高外量子效率和 $2.73 \times 10^{13} \text{ cm} \cdot \text{Hz}^{1/2} \cdot \text{W}^{-1}$ 的归一化探测率,响应时间 t_{on} 为 247 ms, t_{off} 为 266 ms。该探测器制备工艺简单,调控方法也较简单,且性能高,为窄带光电探测器的制备提供了一种新的思路。

参 考 文 献

- [1] de Iacovo A, Venettacci C, Giansante C, et al. Narrowband colloidal quantum dot photodetectors for wavelength measurement applications [J]. *Nanoscale*, 2020, 12 (18): 10044-10050.
- [2] Gao L, Ge C, Li W H, et al. Flexible filter-free narrowband photodetector with high gain and customized responsive spectrum [J]. *Advanced Functional Materials*, 2017, 27 (33): 1702360.
- [3] Lin Q Q, Armin A, Burn P L, et al. Filterless narrowband visible photodetectors [J]. *Nature Photonics*, 2015, 9(10): 687-694.
- [4] Sobhani A, Knight M W, Wang Y M, et al. Narrowband photodetection in the near-infrared with a plasmon-induced hot electron device [J]. *Nature Communications*, 2013, 4: 1643.
- [5] Qin Z L, Song D D, Xu Z, et al. Filterless narrowband photodetectors employing perovskite/polymer synergetic layers with tunable spectral response [J]. *Organic Electronics*, 2020, 76: 105417.
- [6] Wang H Z, Li L, Ma J Q, et al. 2D perovskite narrowband photodetector arrays [J]. *Journal of Materials Chemistry C*, 2021, 9(34): 11085-11090.
- [7] Xue J, Zhu Z F, Xu X B, et al. Narrowband perovskite photodetector-based image array for potential application in artificial vision [J]. *Nano Letters*, 2018, 18(12): 7628-7634.
- [8] Chen Y N, Peng J J, Su D Q, et al. Efficient and balanced charge transport revealed in planar perovskite solar cells [J]. *ACS Applied Materials & Interfaces*, 2015, 7(8): 4471-4475.
- [9] Edri E, Kirmayer S, Mukhopadhyay S, et al. Elucidating the charge carrier separation and working mechanism of $\text{CH}_3\text{NH}_3\text{PbI}_{3-x}\text{Cl}_x$ perovskite solar cells [J]. *Nature Communications*, 2014, 5: 3461.
- [10] 方红华, 黎满泽, 周运科, 等. 钙钛矿中热载流子的超快光谱探测 [J]. *光学学报*, 2021, 41(8): 0823009.
Fang H H, Li X Z, Zhou Y K, et al. Ultrafast spectroscopy of hot carriers in perovskites [J]. *Acta Optica Sinica*, 2021, 41(8): 0823009.
- [11] 杨晔, 杨小丽, 何丽红, 等. 次磷酸增强的准二维钙钛矿天蓝色发光器件 [J]. *光学学报*, 2021, 41(17): 1716001.
Yang Y, Yang X L, He L H, et al. Quasi-two-dimensional sky-blue perovskite light-emitting devices enhanced by hypophosphorous acid incorporation [J]. *Acta Optica Sinica*, 2021, 41(17): 1716001.
- [12] 黄斯豪, 刘征征, 杜鹏, 等. 钙钛矿微纳激光器研究进展 [J]. *激光与光电子学进展*, 2020, 57(7): 071602.
Huang S H, Liu Z Z, Du J, et al. Review of perovskite micro- and nano-lasers [J]. *Laser & Optoelectronics Progress*, 2020, 57(7): 071602.
- [13] 丁楠, 王楠, 刘森, 等. 掺杂卤化物钙钛矿材料研究进展 [J]. *激光与光电子学进展*, 2021, 58(15): 1516011.
Ding N, Wang N, Liu S, et al. Research progress on doped perovskite materials [J]. *Laser & Optoelectronics Progress*, 2021, 58(15): 1516011.
- [14] Jeong M, Choi I W, Go E M, et al. Stable perovskite solar cells with efficiency exceeding 24.8% and 0.3-V voltage loss [J]. *Science*, 2020, 369(6511): 1615-1620.
- [15] Trinh X L, Tran N H, Seo H, et al. Enhanced performance of perovskite solar cells via laser-induced heat treatment on perovskite film [J]. *Solar Energy*, 2020, 206: 301-307.
- [16] 金国君, 徐恺, 檀珺, 等. 具有超低反射率的折射率渐变封装结构 [J]. *光学学报*, 2019, 39(2): 0231001.
Jin G J, Xu K, Tan J, et al. Encapsulation structure of gradient refractive index with ultralow reflectance [J]. *Acta Optica Sinica*, 2019, 39(2): 0231001.
- [17] Geng X S, Wang F W, Tian H, et al. Ultrafast photodetector by integrating perovskite directly on silicon wafer [J]. *ACS Nano*, 2020, 14(3): 2860-2868.
- [18] 林亚楠, 吴亚东, 程海洋, 等. PdSe₂ 纳米线薄膜/Si 异质结近红外集成光电探测器 [J]. *光学学报*, 2021, 41(21): 2125001.
Lin Y N, Wu Y D, Cheng H Y, et al. Near-infrared integrated photodetector based on PdSe₂ nanowires film/Si heterojunction [J]. *Acta Optica Sinica*, 2021, 41(21): 2125001.
- [19] Sun Z H, Aigouy L, Chen Z Y. Plasmonic-enhanced perovskite-graphene hybrid photodetectors [J]. *Nanoscale*, 2016, 8(14): 7377-7383.
- [20] Fang Z Y, Liu Z, Wang Y M, et al. Graphene-antenna sandwich photodetector [J]. *Nano Letters*, 2012, 12 (7): 3808-3813.
- [21] Liu Y, Lang F, Dittrich T, et al. Enhancement of photocurrent in an ultra-thin perovskite solar cell by Ag nanoparticles deposited at low temperature [J]. *RSC Advances*, 2017, 7(3): 1206-1214.
- [22] Liu B, Gutha R R, Kattel B, et al. Using silver nanoparticles-embedded silica metafilms as substrates to enhance the performance of perovskite photodetectors [J]. *ACS Applied Materials & Interfaces*, 2019, 11(35): 32301-32309.
- [23] Pawar E. A review article on acrylic PMMA [J]. *IOSR Journal of Mechanical and Civil Engineering*, 2016, 13(2): 1-4.
- [24] Yuan B L, Li C, Yi W C, et al. PMMA passivated CsPbI₂Br perovskite film for highly efficient and stable solar cells [J]. *Journal of Physics and Chemistry of Solids*, 2021, 153: 110000.
- [25] Zhuang L, Zhang X, Zhang J L, et al. Influence of PMMA thin film combined with Mn-doped cesium lead halide perovskite CsPbCl₃ [J]. *Optical Materials*, 2021, 115: 111050.
- [26] Zhang M D, Lu Q N, Wang C L, et al. High-performance and stability bifacial flexible self-powered perovskite photodetector by surface plasmon resonance and hydrophobic treatments [J]. *Organic Electronics*, 2021, 99: 106330.
- [27] Huang J A, Luo L B. Low-dimensional plasmonic photodetectors: recent progress and future opportunities [J]. *Advanced Optical Materials*, 2018, 6(8): 1701282.
- [28] Mullin J W. *Crystallization* [M]. Amsterdam: Elsevier, 2001.
- [29] Guo H, Jiang L X, Huang K, et al. Unsymmetric squaraine for narrow band green-selective organic photodetectors [J]. *Organic Electronics*, 2021, 92: 106122.
- [30] Li J C, Chen Y F, Zhang B, et al. Non-traditional positively-biased narrow-band perovskite single-crystal photodetectors enabled by interfacial engineering [J]. *Advanced Optical Materials*, 2022, 10(5): 2102225.
- [31] Liu P, Liu Y, Zhang S W, et al. Lead-free Cs₃Sb₂Br₉ single crystals for high performance narrowband photodetector [J]. *Advanced Optical Materials*, 2020, 8(21): 2001072.

Narrow-Band Perovskite Photodetector Based on SPR and Interference Mode Composite Enhancement

He Jiantao^{1,2}, Lu Qieni^{1,2*}, Zhang Mingdi^{1,2}, Dai Haitao^{3,4}, Fu Yikai^{3,4}, Chen Xiaopeng^{1,2}

¹ School of Precision Instrument and Optoelectronics Engineering, Tianjin University, Tianjin 300072, China;

² Key Laboratory of Opto-Electronics Information Technology, Ministry of Education, Tianjin University, Tianjin 300072, China;

³ School of Science, Tianjin University, Tianjin 300072, China;

⁴ Tianjin Key Laboratory of Low Dimensional Materials Physics and Preparing Technology, Tianjin University, Tianjin 300072, China

Abstract

Objective Narrowband photodetectors are widely applied in color image recognition, machine vision, biological sensing, image processing, and other applications. A conventional narrowband photodetector is a combination of a broadband photodetector and a series of optical filters, which significantly increases the device cost, architectural complexity, and energy loss. Therefore, to circumvent this issue, several filter-free approaches are established, including utilization of materials with narrowband absorption, charge collection narrowing (CCN) concept, plasmonic effect, and perovskite/polymer synergetic layers. Among these approaches, perovskite (PVSK) narrowband optoelectronic devices based on metal nanoparticles (MNP) are a topic of significant interest in the fields of solar cells and photodetectors, which incorporate enhanced light via the surface plasmon resonance (SPR) of MNP into the excellent optoelectronic properties of perovskite (high absorption coefficient, long carrier separation distance, high carrier mobility, and adjustable optical broadband). However, the quality of the perovskite film degrades when MNP is integrated with the device that is in direct contact with the perovskite film. One of the ways to solve this problem is to introduce an intermediate layer between PVSK and MNP for film quality. In this study, the polymethylmethacrylate (PMMA) membrane is introduced between perovskite and silver island films, and a new structure of a narrowband enhanced perovskite photodetector is proposed. The device performance can be improved by varying the perovskite precursor solution temperature and thickness of the perovskite.

Methods The narrowband-enhanced perovskite photodetector is fabricated as follows. First, the thin silver film is deposited on a glass substrate via physical vapor deposition, and the silver nanoisland film (Ag NF) is prepared via annealing at 300 °C for 30 min. The average diameter of the Ag NPs is approximately 80 nm. Subsequently, the PMMA intermediate layer is spun on the surface of Ag NF, the perovskite film is spun on the PMMA via spin-coating, and silver electrodes with a thickness of 100 nm are deposited on the perovskite film via thermal evaporation. The narrowband-enhanced perovskite photodetector has a planar structure of SiO₂/Ag NF/PMMA/perovskite. The thickness of the PMMA interlayer is controlled by varying the spin-coating speed and the concentration of the PMMA solution. The grain size and thickness of the perovskite films are governed by the perovskite precursor solution temperature and spin-coating speed, respectively.

Results and Discussions The influence of PMMA thickness on the narrowband bandwidth is investigated in the experiment. The central wavelength of the narrowband response spectrum is approximately 490 nm. The lowest transmissivity decreases with the addition of the PMMA film. The transmissivity first decreases and then increases as the thickness of PMMA increases, where destructive interference occurs via the PMMA film (Fig. 4). The effect of the perovskite precursor solution temperature on the grain size of perovskite films is investigated. The scanning electron microscope (SEM) images (Fig. 5) show that the grain size of the perovskite first increases and then decreases with increasing temperatures, and the maximum grain diameter is ~5 μm at 60 °C, which has the higher photocurrent. Moreover, the thickness of the perovskite film is analyzed under the optimization experimental conditions (temperature of 60 °C, thickness of 278 nm). When the spin-coating speed is 5000 r/min, the maximum photocurrent and large photocurrent gain are obtained (Fig. 6). The performance of the device at optimal parameters (Fig. 7) is characterized. Subsequently, this performance is compared with those of the reported filter-free narrowband photodetectors, as summarized in Table 1.

Conclusions Herein, a narrowband perovskite photodetector based on the surface plasmon resonance of the silver island film is prepared, and the narrowband of the photodetector is enhanced by introducing thin film between the perovskite and silver island films. The grain size of the perovskite films is governed by the perovskite precursor solution temperature,

and the light propagation path is controlled by the thickness of the perovskite to improve the narrowband response. The effects of the PMMA film thickness, precursor solution temperature, and perovskite thickness on the performance of the detector are investigated. The as-prepared photodetector with optimized parameters exhibits a narrow photo-response peak centered at approximately 490 nm with a full width at half maximum of 110 nm, as well as a high responsivity of $0.6 \text{ A} \cdot \text{W}^{-1}$ at an applied bias voltage of 2 V, high external quantum efficiency of 159%, normalized detectivity of $2.73 \times 10^{13} \text{ cm} \cdot \text{Hz}^{1/2} \cdot \text{W}^{-1}$, and response time of 247 ms(rise time)/266 ms(fall time). The detector presented in this paper has a simple fabrication process, particularly in the control method, and exhibits high performance, thus presenting a new strategy for the fabrication of narrowband photodetectors.

Key words measurement; narrow-band photodetector; temperature optimization of precursor solution; surface plasmon resonance; thin film interference